Catalysis Science & Technology

Accepted Manuscript

ROYAL SOCIETY OF CHEMISTRY

www.rsc.org/catalysis

In-built Tb^{4+}/Tb^{3+} Redox Centers in Terbium-doped Bismuth Molybdate Nanograss for Enhanced Photocatalytic Activity

Hongda Li, Wenjun Li*, Shaonan Gu, Fangzhi Wang, Hualei Zhou

Beijing Key Laboratory for Science and Application of Functional Molecular and Crystalline Materials, University of Science and Technology Beijing, Beijing 100083, China

Abstract A series of terbium-doped Bi_2MoO_6 with different Tb content were synthesized using a hydrothermal method. Crystalline structure, surface area, morphology, chemical state and optical properties were analyzed in detail. The photocatalytic activity of the samples were evaluated by degrading organics under visible light irradiation. The results indicated that doping of terbium ions could obviously improve the photocatalytic activity of Bi_2MoO_6, which was attributed to the generation of Tb^{4+} /Tb^{3+} redox centers in terbium-doped Bi_2MoO_6. The photoluminescence (PL) spectroscopy, photocurrent measurement and active species trapping experiments suggest that the recombination of photo-generated electron-hole pairs was efficiently restrained by trapping-releasing process between Tb^{4+} and Tb^{3+} ions.

Keywords: Terbium-doped Bi_2MoO_6, Photocatalysts, Visible light, Degradation

1. Introduction

As a green approach, semiconductor photocatalytic technology has received increasing attention because it can be widely applied to carbon dioxide reduction [1,2], water splitting [3,4] and the decomposition of organics. Undoubtedly, the semiconductor TiO_2 is known as one of the excellent photocatalysts. However, TiO_2 has a wide band gap of 3.2 eV, which responses to UV light that covers only about 4% of the sunlight spectrum, whereas visible light occupies 43% of the solar spectrum. Tremendous effects have been made to exploit new visible-light-driven photocatalysts, such as BiOBr, MoS_2, $BiVO_4$, Bi_2WO_6, Bi_2MoO_6, and so on [5-9].

Bi_2MoO_6 is an active member of the Aurivillius oxide family that has attracted increasing attention because of its luminescence[10], catalytic properties and dielectric[11,12]. Two features make Bi_2MoO_6 standing out among these photocatalysts. Bi_2MoO_6 has the ability of visible light absorption inherently due to the narrow band gap (*ca.* 2.59 eV) [13]. Meanwhile, it has displayed potential photocatalytic performance for the degradation of organic contaminants [14-16]. However,

its application remains limited by the high recombination rate of photo-generated electron-hole pairs in photocatalytic process, and the visible-light response of Bi_2MoO_6 is only less than 500 nm [13,17]. In order to solve these issues, composite materials with a heterojunction structure [18-20], doping of another ions [21,22], and loading noble metal co-catalysts [17,23,24] have been widely investigated. These results indicated that the recombination of photo-generated electron-hole pairs can be effectively restrained under charge transmission, resulting in a high photocatalytic performance. Particularly, the lanthanide ions with 4*f* electron configuration are regarded as effective dopants to improve the photocatalytic activity of Bi_2MoO_6. Alemi [25] reported that doping with Gd^{3+}, Ho^{3+} and Yb^{3+} improved the photocatalytic activities of Bi_2MoO_6 under visible light irradiation. Zhou [22] reported an Er-doped Bi_2MoO_6 synthesized by a simple hydrothermal method, which could up-convert visible light into ultraviolet light to obtain high photocatalytic activity. However, the detailed mechanism of the lanthanide ions doped Bi_2MoO_6 in improving the photocatalytic activity of Bi_2MoO_6 have not yet been entirely understood. And doping of lanthanide ions in Bi_2MoO_6 based on their variable valence has seldom been reported so far as we know.

Terbium is one of the most interesting dopants due to its different electronic structure between Tb^{4+} and Tb^{3+}, leading to different chemical state in crystal lattice. Furthermore, the Tb^{4+} is half-filled in 4*f* orbital that holds 7 *f*-electrons, and this configuration is relatively stable. Herein, we reported a grass-like terbium-doped Bi_2MoO_6 photocatalysts prepared by a hydrothermal method for the first time. An obvious red shift of the optical absorption edge for the doped samples as compared to Bi_2MoO_6. The rhodamine B (RhB), phenol and methylene blue (MB) were used to evaluate the photocatalytic activity of the as-prepared samples under visible-light irradiation. The results indicated that Tb-doped Bi_2MoO_6 exhibits an obvious enhancement on photocatalytic property compared to Bi_2MoO_6. Moreover, the plausible mechanism of the enhanced photocatalytic activity was discussed in detail.

2. Experimental

2.1. Synthesis of the photocatalysts

Tb-doped Bi_2MoO_6 (Tb-BMO) was prepared through a hydrothermal process. The details were as follows: $Bi(NO_3)_3 \cdot 5H_2O$ (2 mmol) and $(NH_4)_6Mo_7O_{24} \cdot 4H_2O$ (0.14 mmol) were respectively dissolved in 40 mL of 2 mol L^{-1} nitric acid solution and 40 mL deionized water under vigorous magnetic stirring at room temperature. Then, these two solutions were mixed together and stirred at room temperature for 40 min. Subsequently, different amount of $Tb(NO_3)_3$ solutions (Tb: Bi = 0 at.%, 0.5 at.%, 1.0 at.%, 1.5 at.%, 2.0 at.%, 2.5 at.%, 3.0 at.% and 3.5 at.%) were added into the

above solution respectively. And the pH of these suspensions were adjusted to about 9 using ammonia solution. After stirring for 30 min, the suspensions were added into 100 mL Teflon-lined stainless autoclave and heated at 180 °C for 12h. Then, the products cooled to room temperature naturally, followed by been collected via filtration and washed with deionized water for several times, and finally dried at 80℃ for 8 h.

2.2. Characterization

The crystalline phases of samples were analyzed using X-ray diffraction (XRD) (D/MAX-RB, Rigaku, Japan). The diffraction patterns were recorded in the 2θ range of 20–80°with a Cu Kα source (λ=0.15405) running at 40 kV and 30 mA. Raman spectra were recorded by Raman spectrometer (Horiba LabRam, T64000, France) at 532 nm excitation wavelengths. The specific surface area of samples were determined by Brunauer–Emmett–Teller (BET) method (NOVA 4200e, Quantchrome, USA). The morphology of the as-prepared samples were measured by using scanning electron microscopy (SEM) on a SUPRA 55 SAPPHIRE instrument operating at 20 kV. The high-resolution transmission electron microscopy (HRTEM) images were investigated by a transmission electron microscopy (F-20, FEI, USA) at accelerating voltage of 200 kV. X-ray photoelectron spectroscopy (XPS) was performed on an X-ray photoelectron spectrometer (ESCALAB 250Xi) using the Al Kα radiation. The UV–vis diffuse reflectance spectra (DRS) of the photocatalysts were recorded in air at room temperature in wavelength range of 300–600 nm using a UV–vis spectrophotometer (U-3900H, Hitachi, Japan) equipped with an integrating sphere. The photoluminescence (PL) spectra were carried out on a fluorescence spectrophotometer (F-4500, Hitachi, Japan) with a Xe lamp as the excitation light source.

2.3. Photocatalytic experiment

Photocatalytic degradation of organics (RhB (10 mg L^{-1}), phenol (20 mg L^{-1}) and MB (10 mg L^{-1})) were performed under visible light (λ >420 nm, 400W Xe lamp). 40 mg of as-prepared samples were dispersed in 40 mL of organics aqueous solution followed by stirring for 60 min in the dark to get an adsorption-desorption equilibrium between the samples and organics. During the irradiation, 3 mL of the dispersion samples were collected at 60 min intervals and centrifuged to obtain the supernatants. The absorbance of the as-obtained supernatants were tested using a UV–vis spectrophotometer (U-3900H, Hitachi, Japan) at 553 nm, 269 nm, 664 nm respectively, and the radio (C/C_0) of the organics concentration was adopted to evaluate the degradation efficiency, where C was the organics concentration at certain time and C_0 was the organics concentration at the time of the adsorption-desorption equilibrium.

2.4. Photocurrent measurement

The measurement of the photocurrent was carried out on an electrochemical workstation (5060F, RST, China) in a standard three-electrode system with the samples, an Ag/AgCl electrode (saturated KCl), and a Pt wire used as the working electrode, reference electrode, and counter electrode, respectively. And a 0.5 mol L^{-1} Na_2SO_4 aqueous solution was introduced as electrolyte. A 100 W incandescent lamp with a 420 nm cut off filter was used as the light source. For the preparation of the working electrode, 3 mg samples were dispersed in a certain amount of ethanol and Nafion on solution homogeneously. The as-prepared samples were spread on the bottom middle of an ITO glass in a circle with a diameter of 6 mm. The photocurrents of the photocatalysts with the light on and off were measured at 0.8 V.

3. Results and discussion

3.1. XRD and Raman analysis

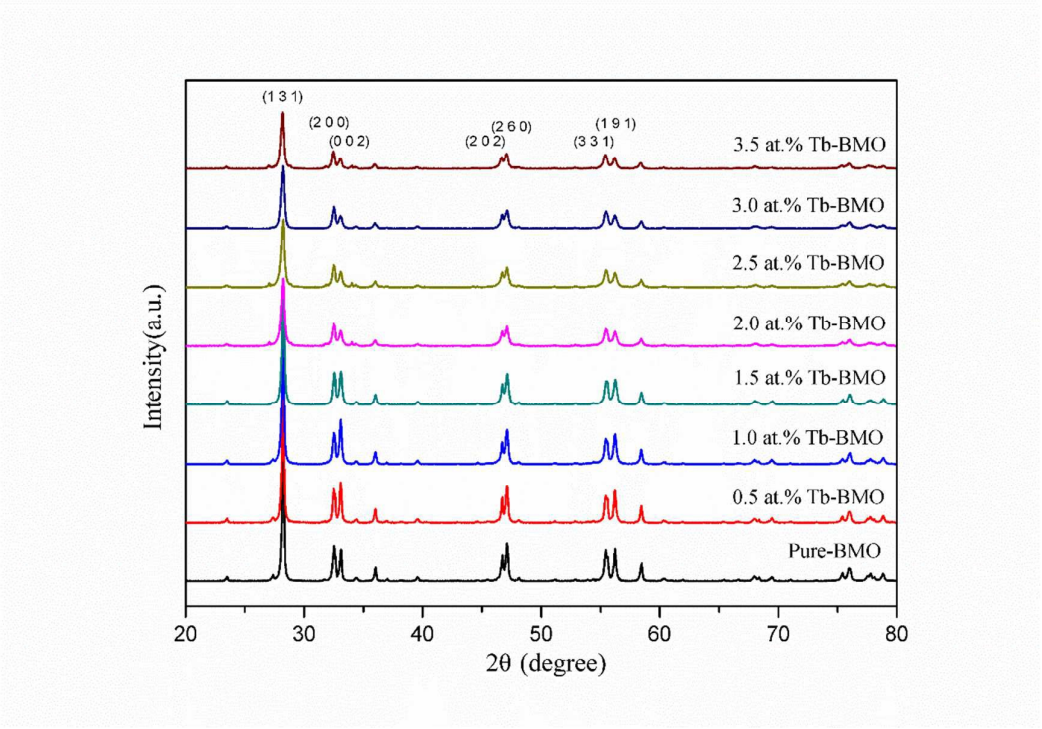

Fig. 1. XRD patterns of the pure BMO, 0.5 at.%, 1.0 at.%, 1.5 at.%, 2.0 at.%, 2.5 at.%, 3.0 at.% and 3.5 at.% Tb-BMO samples synthesized by hydrothermal reaction at 180℃ for 12 h.

Table 1. Surface area, crystal sizes and lattice parameter of the pure BMO and Tb-BMO series of samples

Samples	Surface Area ($m^2 g^{-1}$)	Crystal Vol ($Å^3$)	Lattice Parameters		
			a (Å)	b (Å)	c (Å)
pure BMO	16.861	489.62	5.501	16.223	5.487
0.5 at.% Tb-BMO	16.472	490.06	5.501	16.223	5.491
1.0 at.% Tb-BMO	15.617	490.19	5.500	16.225	5.493
1.5 at.% Tb-BMO	15.443	489.67	5.498	16.218	5.492
2.0 at.% Tb-BMO	14.912	489.81	5.498	16.220	5.492
2.5 at.% Tb-BMO	17.312	490.04	5.499	16.231	5.490
3.0 at.% Tb-BMO	15.590	490.40	5.502	16.226	5.493
3.5 at.% Tb-BMO	12.257	491.37	5.505	16.238	5.497
Tb_2MoO_6[26]	—	1072.12	7.71	11.29	7.71

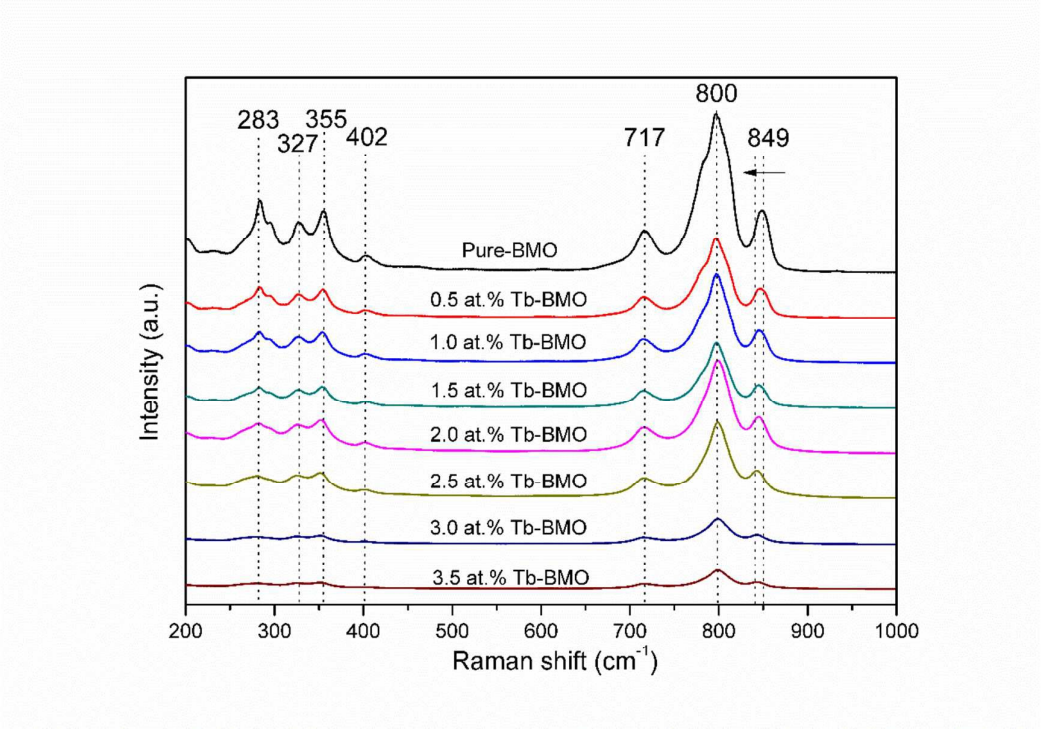

Fig. 2. Raman spectra of pure BMO, 0.5 at.%, 1.0 at.%, 1.5 at.%, 2.0 at.%, 2.5 at.%, 3.0 at.% and 3.5 at.% Tb-BMO

Fig.1 shows the typical diffraction patterns of the synthesized samples. It revealed that all the samples had a Koechlinite Bi_2MoO_6 structure and the major diffraction peaks at 2θ values of 28.2°, 32.5°, 33.1°, 46.7°, 47.1°, 55.5°, and 56.2°were respectively indexed as (1 3 1), (2 0 0), (0 0 2), (2

0 2), (2 6 0), (3 3 1), and (1 9 1) planes of the gamma phase of bismuth molybdate (JCPDS card number 21-0102). No signals for any crystalline phases of terbium oxides were observed in the as-prepared photocatalysts because of their low Tb content [19]. The intensity of XRD mainly related with the degree of crystallinity, while doping impurity irons into crystalline structure would decrease the crystallinity. Therefore, the peak intensities of the doped samples decreased in comparison to pure BMO, indicating that the degree of the cationic ordering was declined by the doping of terbium. This implies that terbium ions have successfully replaced partial Bi^{3+} ions in the lattice of Bi_2MoO_6.

In order to further explore the change of the crystalline phases, the lattice parameters and cell volumes of the pure BMO and Tb-BMO were calculated from the XRD data and listed in table.1. It can be found that the cell parameters of Tb-BMO samples increased as a whole with the increasing content of Tb. Meanwhile, the result of XRD analysis showed that the crystal phase of Bi_2MoO_6 did not change after doping of Tb. According to the *Vegard's law*[27], the crystal volumes of Tb-doped Bi_2MoO_6 should be the values between the crystal volume of Bi_2MoO_6 (489.62 $Å^3$) and Tb_2MoO_6 (1072.12 $Å^3$) as the result of the substitution of Tb for Bi^{3+}ions in $(Bi_2O_2)_n^{2+}$ layers of Koechlinite Bi_2MoO_6, though the substitution of smaller rare-earth ions Tb^{4+} (76 pm) or Tb^{3+} (104 pm) for the larger Bi^{3+} (117 pm) ions [28,29].

Furthermore, the crystal structure of as-prepared photocatalysts were characterized by Raman spectroscopy as shown in Fig.2, where characteristic bands of γ-Bi_2MoO_6 were observed [30]. The pure BMO showed a strong band at 800 cm^{-1} and two medium intensity bands at 717 cm^{-1} and 849 cm^{-1}, corresponding to the Mo–O stretching modes of distorted MoO_6 octahedron in Bi_2MoO_6 [31]. The bands with lower intensity located at 283 cm^{-1}, 327 cm^{-1}, 355 cm^{-1}, and 402 cm^{-1} were also confirmed to belong to O−Mo−O bending motions [32]. Both the decline of the peak intensity and the broadening of peak for the doped photocatalysts with the increasing of the Tb content, suggesting the deformation of the crystal structure after doping[33,34]. In addition, apparent red shift of peaks at about 849cm^{-1} was observed depending on the doping levels of the terbium in the BMO crystal lattice, which indicated that the doped terbium mainly influenced the octahedral structure of MoO_6.

3.2. Morphology characterization and BET surface area analysis

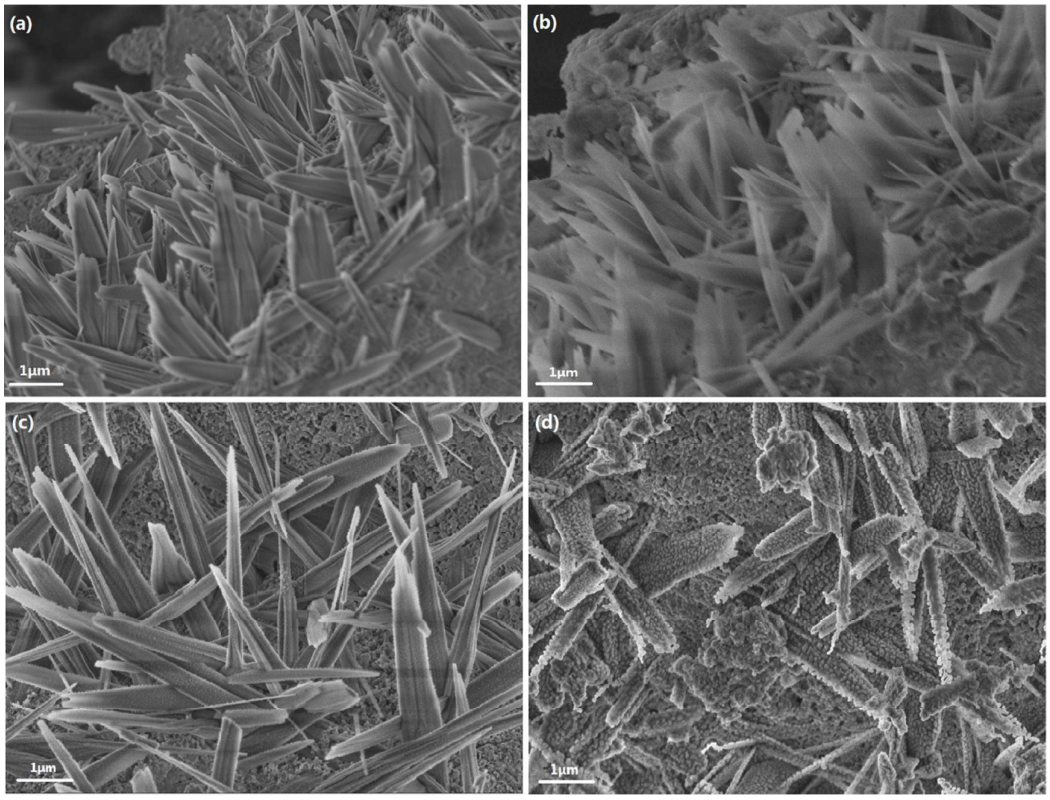

Fig. 3. SEM images of (a) pure BMO, (b) 2.0 at.% Tb-BMO (c) 3.0 at.% Tb-BMO and (d) 3.5 at.% Tb-BMO.

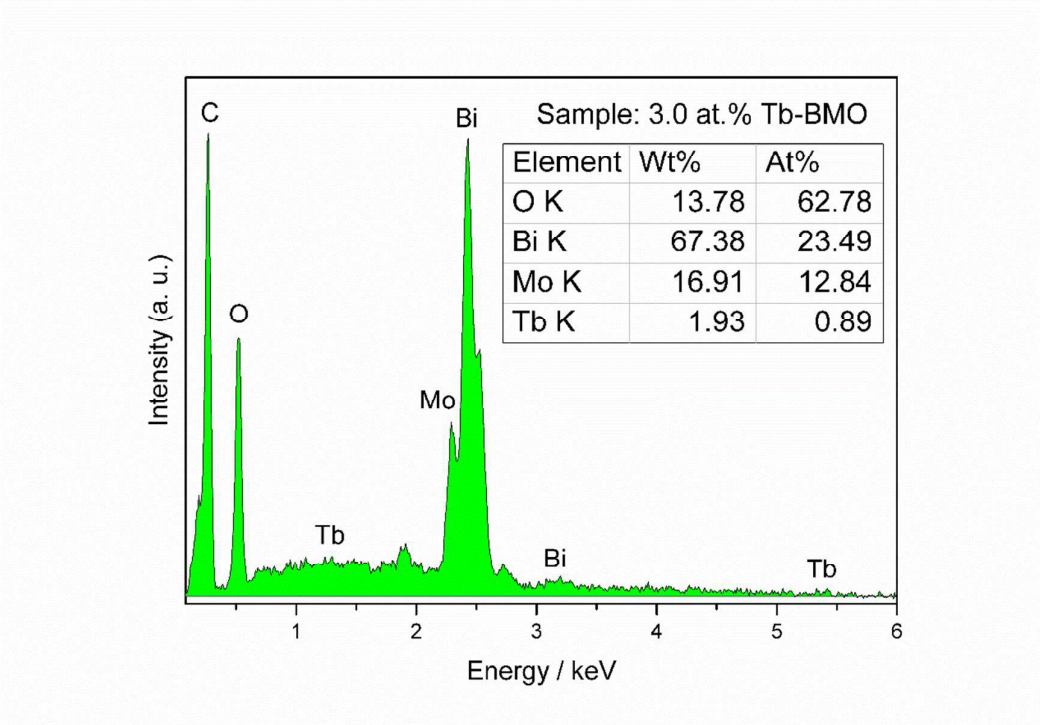

Fig. 4. EDX spectrum of 3.0 at.% Tb-BMO sample

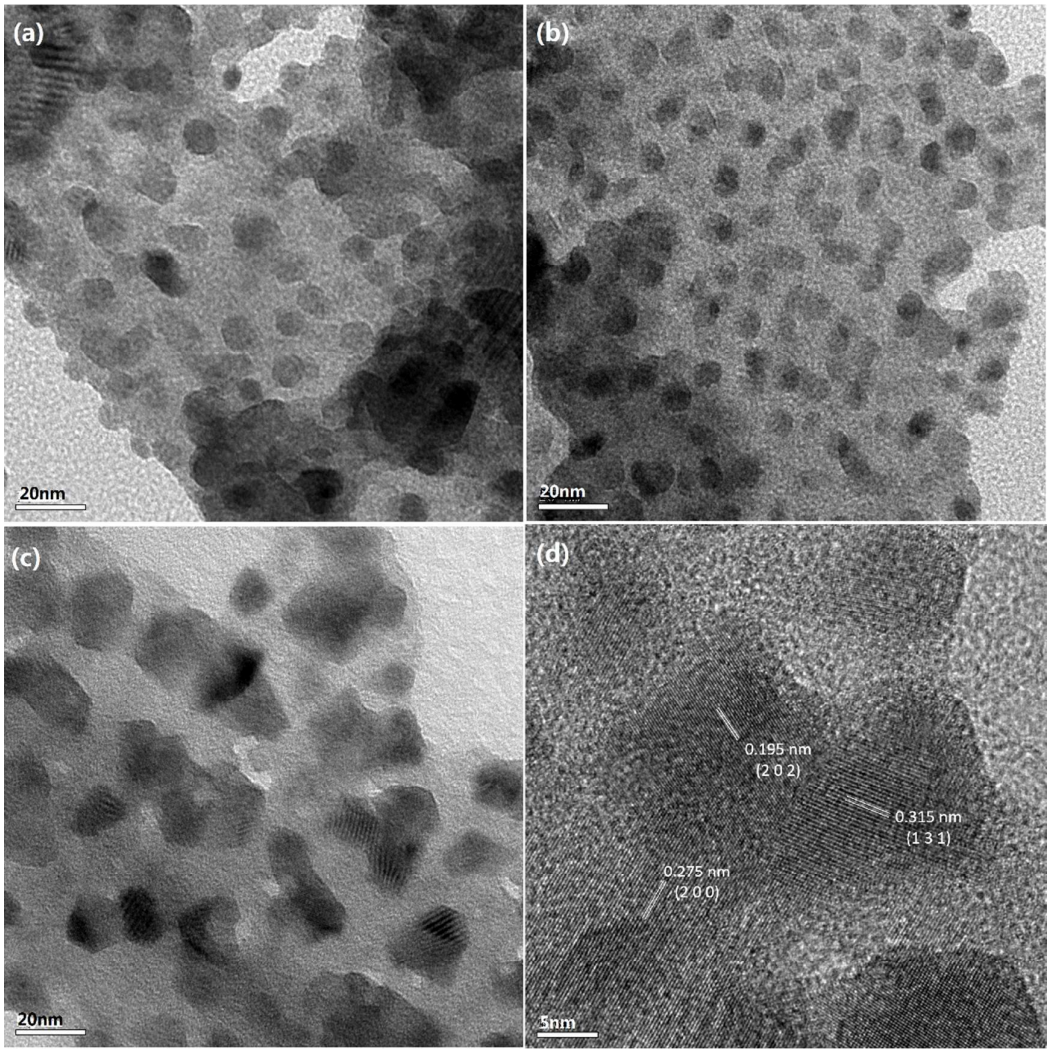

Fig. 5. TEM images of (a) pure BMO, (b) 2.0 at.% Tb-BMO, (c) 3.0 at.% Tb-BMO and HRTEM image of (d) 3.0 at.% Tb-BMO.

Fig. 3 shows the SEM images of (a) pure BMO, (b) 2.0 at.% Tb-BMO (c) 3.0 at.% Tb-BMO and (d) 3.5 at.% Tb-BMO. The pure BMO has a grass-like morphology covered by uniform nano-spheres, and the average width of the nanograss BMO was about 500 nm (Fig. 3a). The surface area of such pure BMO was tested to be16.861 $m^2 g^{-1}$ (Table 1). Doping terbium ions did not change the nanograss morphology but made obvious influence on the distribution of those surface dots (Fig. 3(c, d)). The size of nano-spheres significantly increased with increasing Tb doping levels. Table 1 also shows that the surface area of the samples decreased to 16.472 $m^2 g^{-1}$, 15.617 $m^2 g^{-1}$, 15.443 $m^2 g^{-1}$, 14.912 $m^2 g^{-1}$, 15.590 $m^2 g^{-1}$ and 12.257 $m^2 g^{-1}$ respectively when the terbium content was 0.5 at.%, 1.0 at.%, 1.5 at.%, 2.0 at.%, 3.0 at.% and 3.5 at.%, corresponding to the size of micro region. An interesting point is that the 2.5 at.% Tb-BMO has highest specific

surface area (17.312 m^2/g) and the 3.5 at.% Tb-BMO has minimum surface area. These results demonstrated that the surface area of BMO materials increased with appropriate dopant concentration. Fig. 4 shows the EDX spectrum of 3.0 at.% Tb-BMO sample. The obvious signals for C, O, Bi, Mo and Tb elements can be detected, and C element derived from the carbon conductive membrane. From the inset, it can be found that the molar ratio of (Bi + Tb): Mo is 24.38: 12.84, which is nearly in keeping with the theoretical calculating value. Meanwhile, 3.79 at.% of the molar ratio of Tb: Bi approximate to the value of calculation (3.0 at.%). Therefore, the spectrum and inset can collectively explain that terbium ions have been introduced into Bi_2MoO_6 lattice.

The HRTEM was used to confirm the component of nano-spheres on the surface of nanograss. Fig. 5 shows the TEM images of (a) pure BMO, (b) 2.0 at.% Tb-BMO, (c) 3.0 at.% Tb-BMO and HRTEM image of (d) 3.0 at.% Tb-BMO. Those nano-spheres with an average diameter of about 10 nm originally existed and tightly attached onto the surface of the BMO nanograss (Fig. 5a). Doping Tb gave rise to the significant growth of the nano-spheres in size up to 20nm diameter (Fig. 5c). The interplanar spacing of 0.315, 0.275 and 0.195 nm recorded in Fig. 5d agree well with the (1 3 1), (2 0 0) and (2 0 2) lattice planes of the koechlinite Bi_2MoO_6, respectively. Therefore, both the nano-spheres and nanograss were proved to be crystalline BMO, and doping terbium ions just improved the growth of Bi_2MoO_6 nano-spheres on the surface of the Bi_2MoO_6 nanograss.

3.3. Chemical state analysis

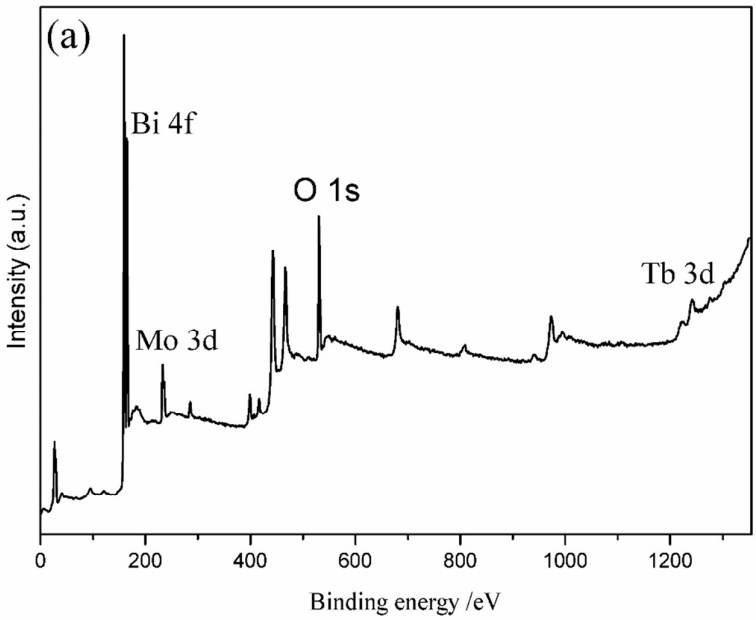

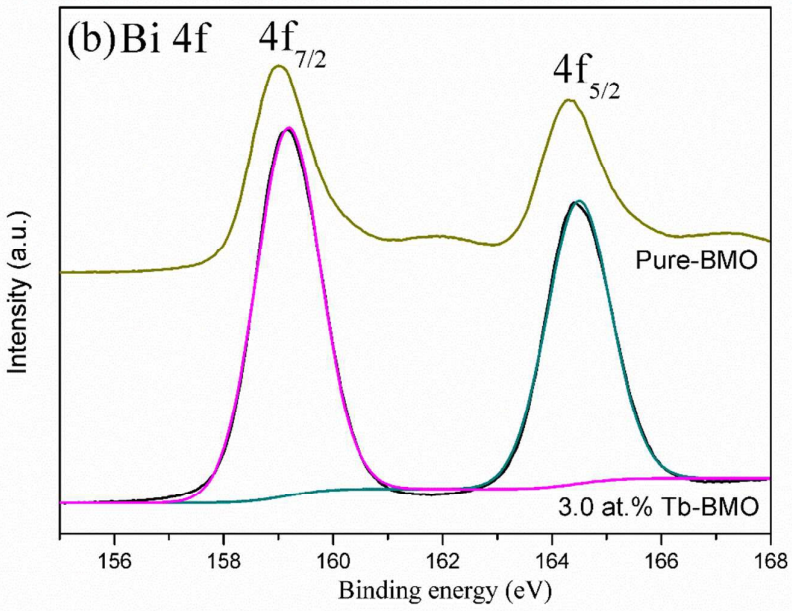

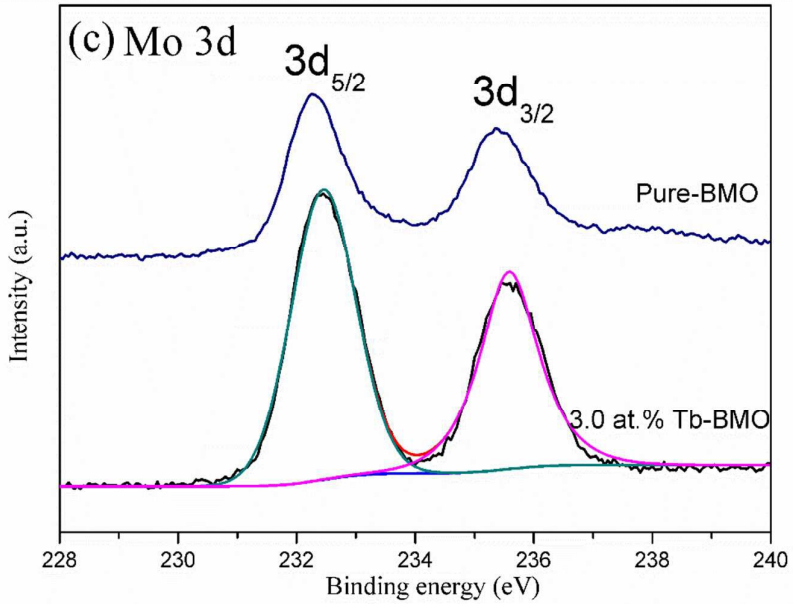

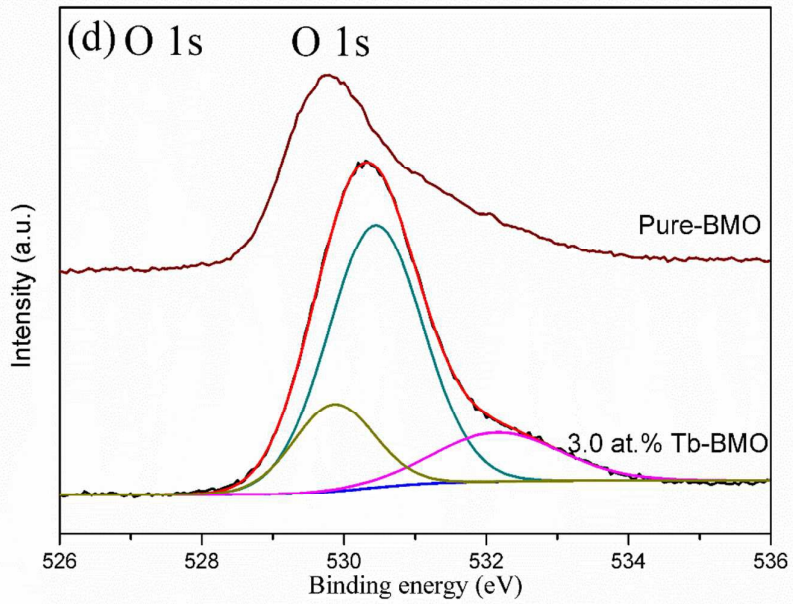

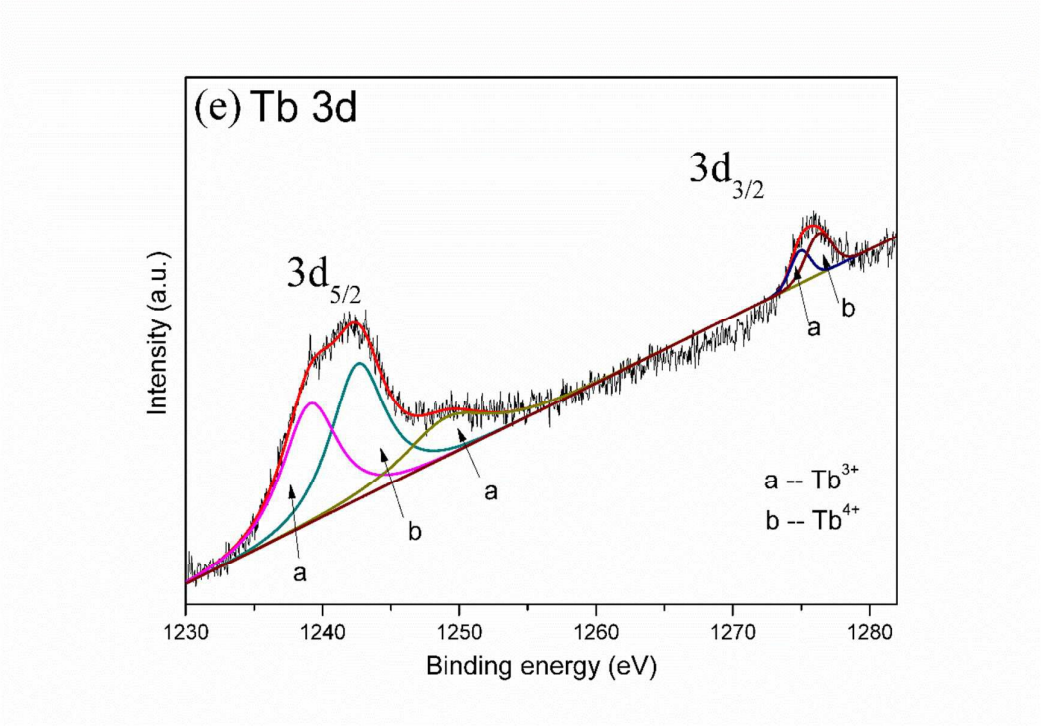

Fig. 6. XPS spectra: (a) overall spectra of 3.0 at.% Tb-BMO; (b-d) Bi 4*f*, Mo 3*d*, O 1*s* of pure BMO and 3.0 at.% Tb-BMO; (e) Tb 3*d* of 3.0 at.% Tb-BMO.

The chemical states of pure BMO and 3.0 at.% Tb-BMO were investigated by XPS and were calibrated using C 1*s* peak at 284.8 eV before analysis. The overall XPS spectra of 3.0 at.% Tb-BMO displayed the characteristic peaks of the Bi, Tb, Mo and O elements (Fig. 6a). As shown in Fig. 6b, the XPS signals located at 159.18 eV and 164.49 eV were attributable to Bi $4f_{7/2}$ and Bi $4f_{5/2}$, respectively, corresponding to a Bi^{3+} cation. While the peaks at 232.45 eV and 235.58 eV were assigned to Mo $3d_{5/2}$ and $3d_{3/2}$ orbitals of Mo^{6+} cations in the crystal lattice (Fig. 6c) [35]. And it can be found that Bi 4*f* and Mo 3*d* of 3.0 at.% Tb-BMO have not obvious displacement compared to pure BMO. For oxygen (Fig. 6d), the fitting peaks were attributed to the Bi-O at 529.87 eV, the Mo-O at 530.43 eV, and the H-O at 532.18 eV, respectively [36,37]. It need to be noticed that the binding energy of O 1*s* reduces from 530.36 eV to 529.85 eV, which was attributed to the formation of Tb–O–Bi bonds [38]. The XPS signals of Tb 3*d* are complicated because of the hybridization of the Tb 4*f* orbital with ligand orbital and fractional occupancy of the valence 4*f* orbital. The characteristic peaks of Tb 3*d* region were generally centered at around 1242.41 eV and 1275.79 eV, corresponding to Tb $3d_{5/2}$ and $3d_{3/2}$, respectively [39]. With fitting (Fig. 6e), we clearly see the separated doublets for Tb^{3+}(1239.09 eV and 1274.94 eV) and Tb^{4+}(1242.59 eV and 1276.28 eV), respectively. The relatively intense peak at 1249.12 eV was assigned to the $3d_{5/2}$ of Tb^{3+} [40,41]. In addition, the fitting peak areas in the same orbital peak of XPS could

semi-quantitatively calculate the ratio of corresponding valence states ions [37]. Therefore, it can be calculated that the content ratio of Tb^{3+}:Tb^{4+} is 1.25:1 according to the peak area of Tb 3*d*. These results demonstrated that the mixed valence states of the terbium species (+3 and +4) in the Tb-BMO photocatalysts.

3.4. Optical properties

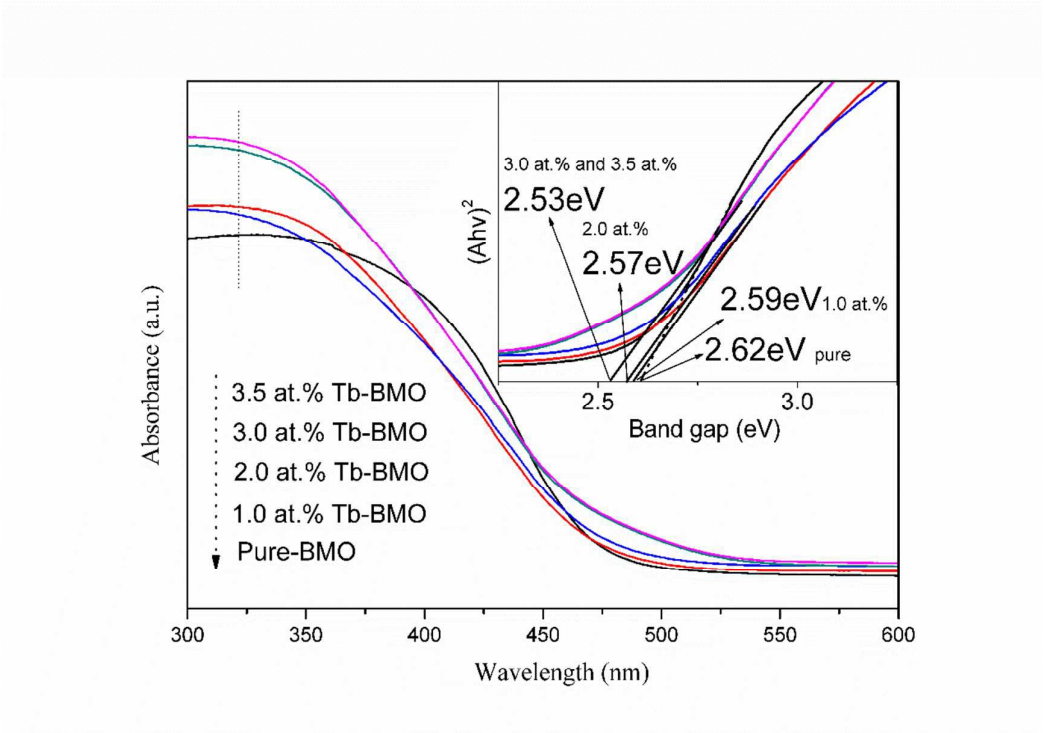

Fig. 7. UV-vis DRS spectra of pure BMO, 1.0 at.% Tb-BMO, 2.0 at.% Tb-BMO, 3.0 at.% Tb-BMO and 3.5 at.% Tb-BMO; the inset shows the band gap energy of the corresponding photocatalysts.

The optical properties of the pure BMO and Tb-BMO were measured using a UV-vis diffusion-reflection spectrometer in the wavelength rang of 300-600 nm (Fig.7). Apparently, doping terbium significantly affected the light absorption property of the pristine BMO. An obvious red shift of the optical absorption edge was observed for the doped samples. The optical band gap for the semiconductor photocatalysts was estimated using the following equation:

$$Ah\nu = \alpha(h\nu - Eg)^{n/2}$$

in which α, ν, A, and Eg represent the absorption coefficient, light frequency, proportionality constant, and band gap, respectively, and n equals 1 or 4, depending on whether the transition is direct or indirect [42]. Bi_2MoO_6 has a direct band gap, and n was 1 herein [43]. The inset of Fig.5 shows the curve of $(\alpha h\nu)^2$ versus hν for as-prepared samples. The band gaps for pure BMO, 1.0 at.% Tb-BMO, 2.0 at.% Tb-BMO, 3.0 at.% Tb-BMO and 3.5 at.% Tb-BMO were calculated to be

about 2.62eV, 2.59 eV, 2.57eV, 2.53eV and 2.53eV, respectively. The result indicated that like other dopants Tb doping works to extend the light absorption of BMO to longer wavelengths.

3.5. Photocatalytic property

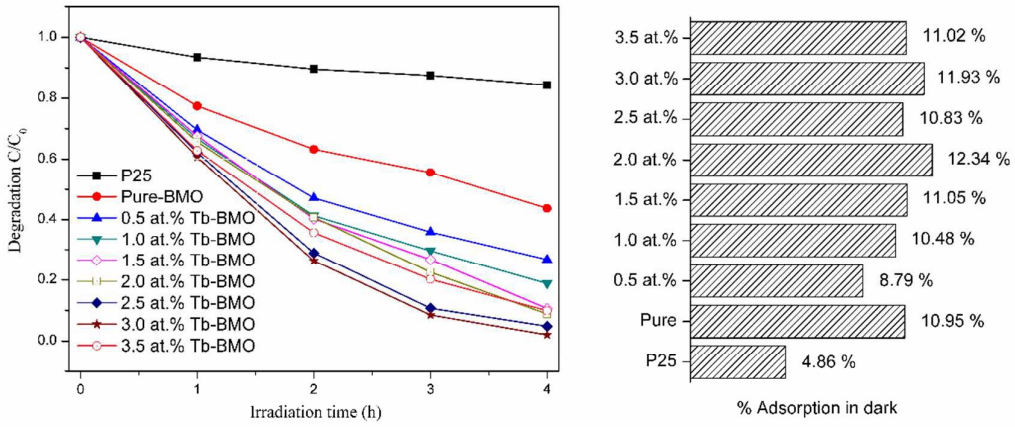

Fig. 8. Comparison of the adsorption and degradation ratio of RhB using the P25, pure BMO and Tb-BMO series of samples in dark and under visible light irradiation

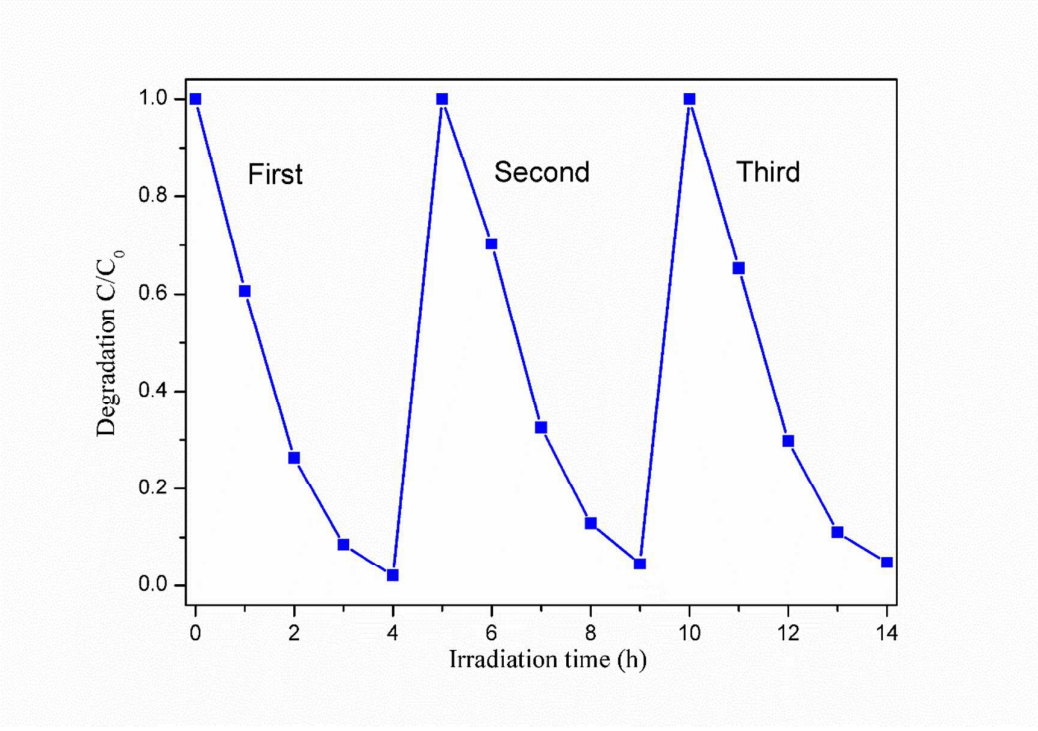

Fig. 9. Circulating runs in the photocatalytic degradation of RhB in the presence of 3.0 at.% Tb-BMO sample

under visible light irradiation

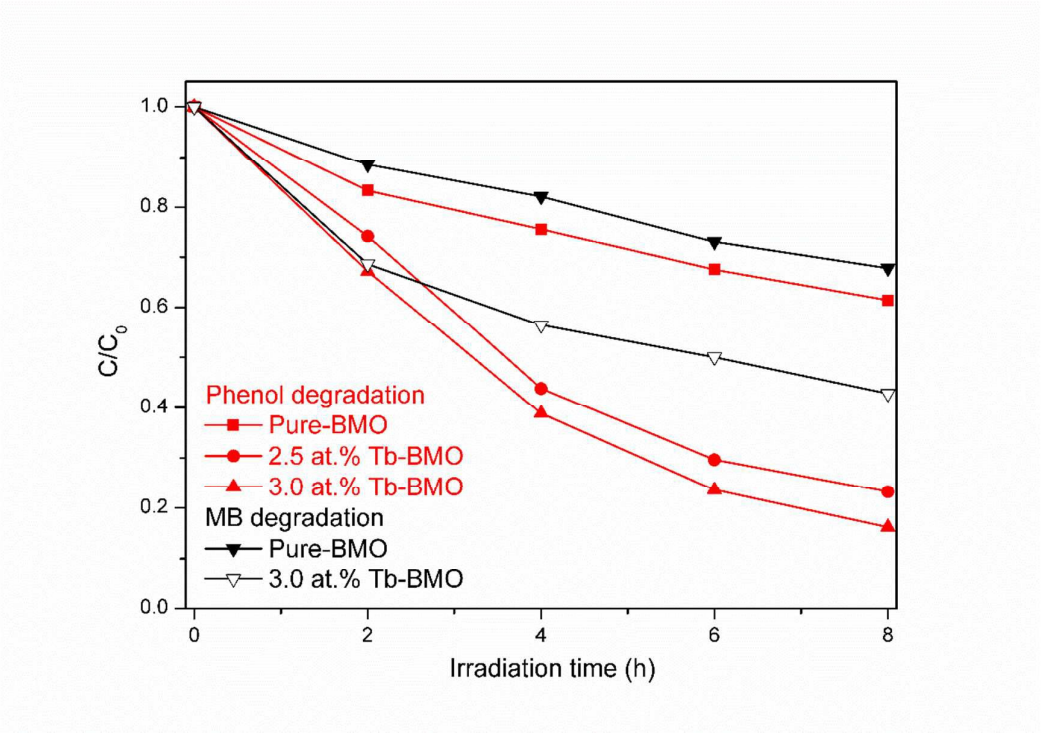

Fig. 10. Photocatalytic degradation of phenol (40 mL, 20 mg L^{-1}) and MB (40 mL, 10 mg L^{-1}) over 0.04 g of samples under visible light irradiation

The photocatalytic performances of the pure BMO and Tb-BMO were evaluated by decomposing rhodamine-B (RhB) in aqueous solution under visible light irradiation (Fig. 8). Generally, the different concentration of RhB adsorbed on the catalyst surface will have a great influence on the photocatalytic performance, so the adsorption ratio was collected when adsorption-desorption equilibrium was achieved before irradiation. Fig. 8 shows that all samples presented the similar capacity for RhB adsorption, though having different surface area. In addition, it can be seen that the photocatalytic activity of the Tb-doped samples was obviously higher than that of the pure BMO samples, and the best activity was obtained for 3.0 at.% Tb-BMO. After 4 hours irradiation, the photodegradation rate of RhB reached up to 98.0% for 3.0 at.% Tb-BMO which was about 1.74 times in comparison to that of pure BMO (56.3%), while 0.5 at.%, 1.0 at.%, 1.5 at.%, 2.0 at.% and 2.5 at.% samples reach the rates up to 73.3%, 81.2%, 89.4%, 91.2% and 95.2%, respectively. Moreover, the photodegradation ratio of RhB decreased to 90.1% for 3.5 at.% Tb-BMO, which demonstrated that further increasing the terbium content in the Bi_2MoO_6 will result in decreasing of the photocatalytic activity under visible light irradiation. The plausible reason is that extra terbium ions might be the recombination center of the photo-generated electron-hole pairs [19]. The results confirmed that the doping of terbium played an

important role in the enhancement of photocatalytic activity of Bi_2MoO_6.

In our work, the circulating runs in the photocatalytic degradation of RhB were performed under visible light irradiation to check the stability of the best photocatalyst (3.0 at.% Tb-BMO). As shown in Fig. 9, the photocatalyst did not display any significant loss of photocatalytic performance. This result implied that the Tb-doped Bi_2MoO_6 photocatalysts are not photo-corroded during the photo-degradation of the pollutant molecules, which is particular important for its application.

Phenol and MB showed the characteristic absorption at the wavelength of 269 nm [44] and 664 nm respectively. Fig. 10 represents the photocatalytic activity of the prepared Tb-BMO samples were evaluated by examining the photo-degradation of phenol (20 mg L^{-1}) and MB (10 mg L^{-1}) respectively under visible light irradiation. It can be observed that about 38.6% of phenol has been degraded over the pure BMO sample when irradiated for 8 hours. And this percentage were even increased to 76.8% and 83.8% over the 2.5 at.% Tb-BMO and 3.0 at.% Tb-BMO samples, respectively. Meanwhile, the pure-BMO and 3.0 at.% Tb-BMO show 32.2% and 57.2% degradation ratio for MB respectively after 8 hours under visible light irradiation. Accordingly, 3.0 at.% Tb-BMO showed a much higher photocatalytic activity for both phenol and MB which were about 2.17 and 1.78 times in comparison to that of pure BMO.

3.6. Photocatalytic Mechanism of Tb-BMO

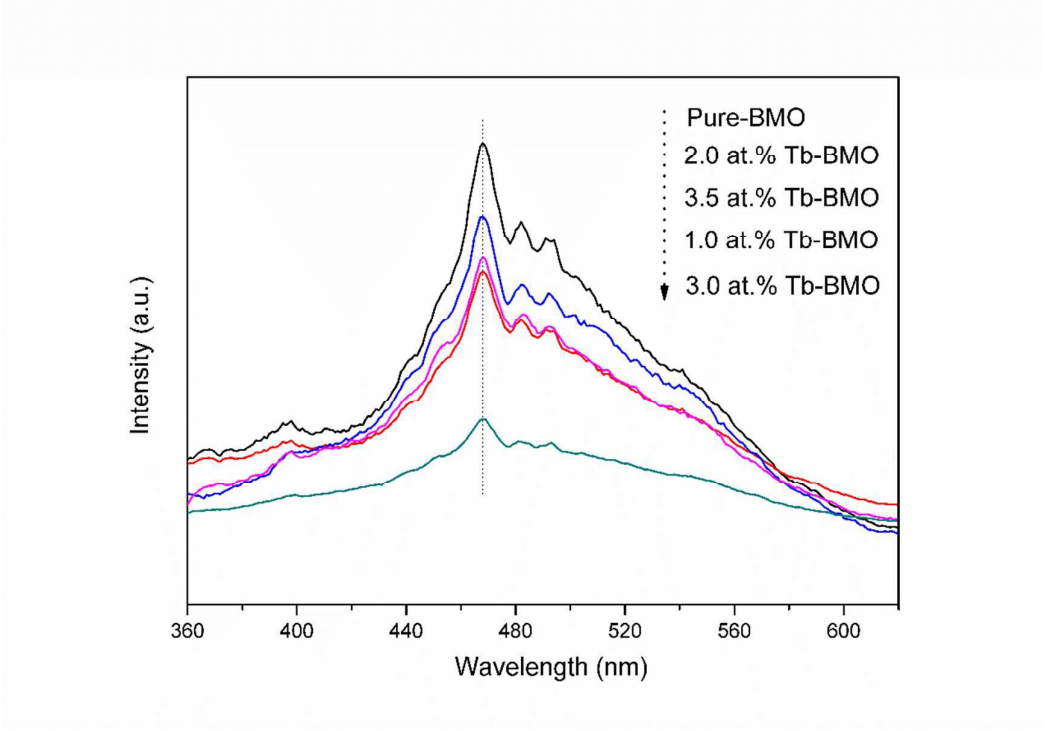

Fig. 11. Photoluminescence (PL) spectra of pure BMO and Tb-BMO series.

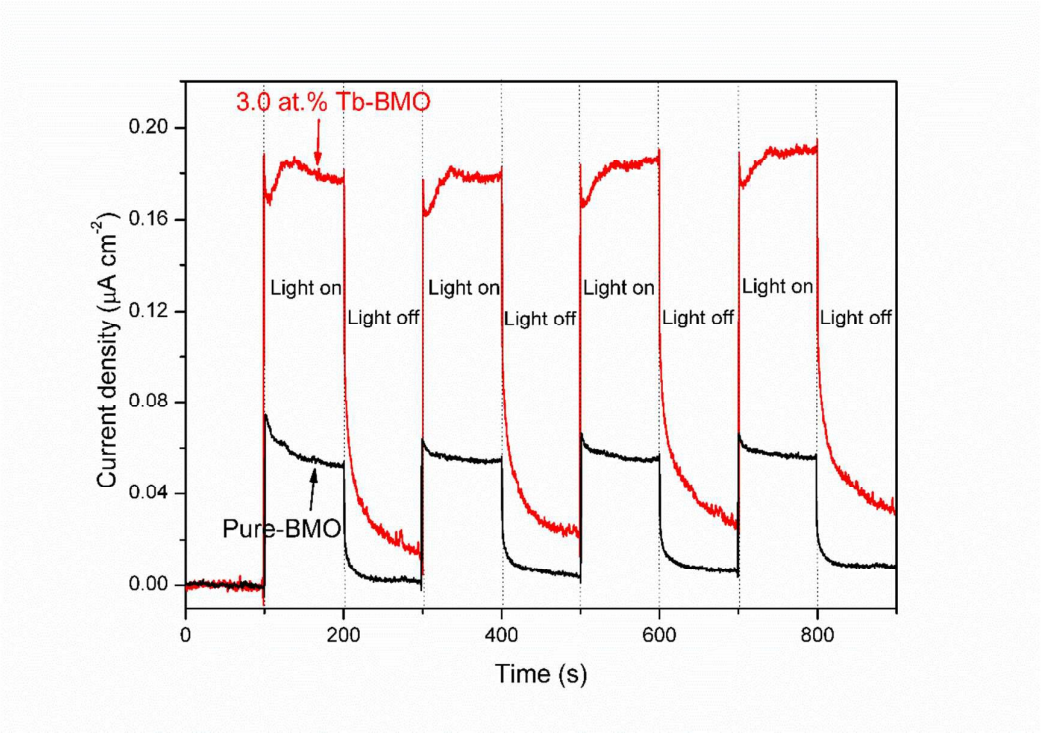

Fig. 12. Photocurrent responses of pure BMO and 3.0 at.% Tb-BMO samples under visible light irradiation.

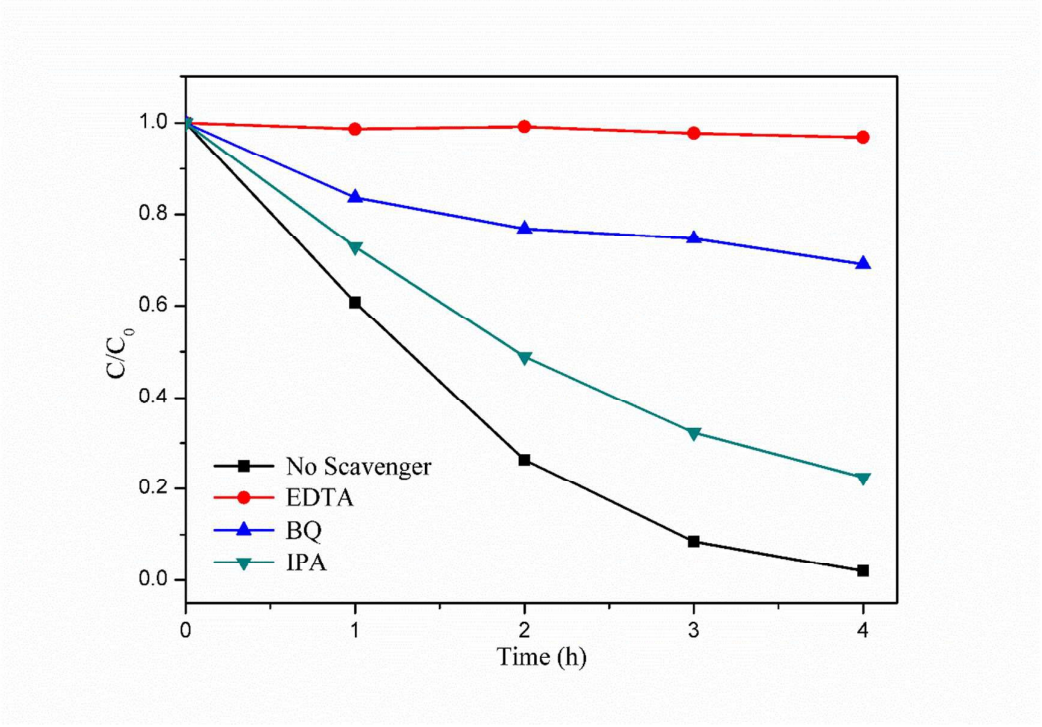

Fig. 13. Photocatalytic degradation of RhB over the 3.0 at.% Tb-BMO photocatalyst with the addition of scavengers EDTA, BQ and IPA.

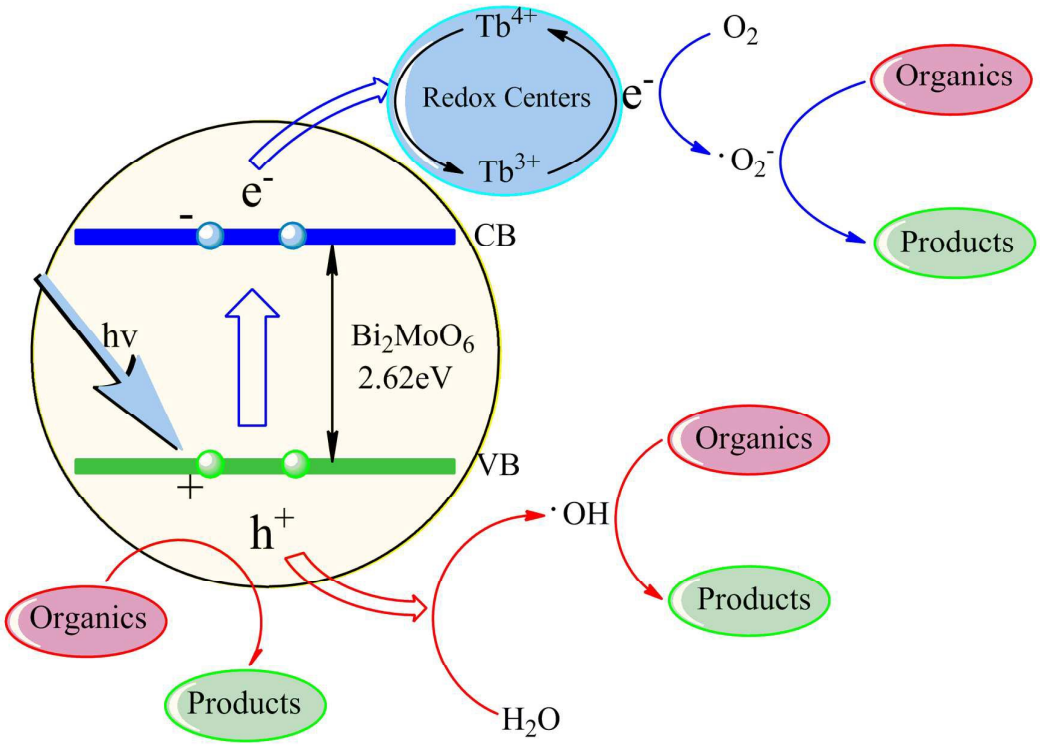

Fig.14. Schematic illustration of the mechanism of Tb-BMO photocatalyst under visible light irradiation

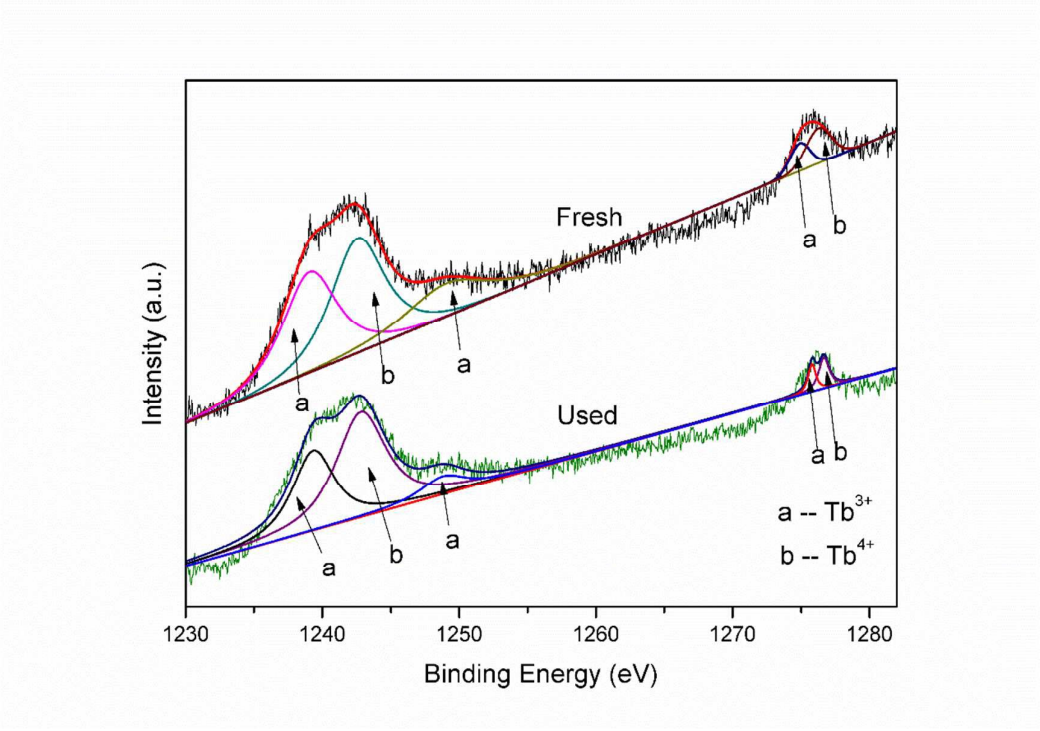

Fig. 15. XPS of terbium in 3.0 at.% Tb-BMO before and after photocatalytic reaction

Overall the photocatalytic activity of BMO was highly improved with Tb doping. As discussed

above, such enhancement may partially come from the enhanced light absorption, increased BET surface area and the improved charge separation. 3.0 at.% Tb-BMO sample exhibits the best performance but with lower BET than both 2.5 at.% Tb-BMO and pristine BMO, and weaker light absorption compared to 3.5 at.% Tb-BMO. It is clear that both light absorption and surface area related benefits are weak in this study. Therefore, the main enhancement mechanism is possibly attributed to the improved charge separation due to the presence of the in-built Tb^{4+}/Tb^{3+} redox centers that facilitates the charge transfer and suppresses the charge recombination in the BMO bulk. To confirm this, PL spectrum was carried out in the range of 360-620 nm for pure BMO and Tb-BMO series (Fig. 11). It can be observed that the PL intensities of the Tb-BMO photocatalysts were obviously weaker than that of pure BMO, and the lowest peak intensity was observed for 3.0 at.% Tb-BMO. Generally, the lower PL intensity indicates the stronger charge separation and thus the lower recombination rate of the photo-generated electron-hole pairs, which leads to the higher photocatalytic performance of semiconductor materials [45]. Unlike the typical transition metals doped semiconductors for photocatalysis where dopants introduce more recombination centers to consume the charge carriers, Tb doping in BMO results in the generation of in-built Tb^{4+}/Tb^{3+} pairs that act as redox center to facilitate the charge separation and restrain the recombination.

The photocurrent responses of the samples in an electrolyte under visible light irradiation directly correlate with the generation and transfer of the photo-generated charge carriers in the photocatalytic process, which can further confirm the separation of electron–holes pairs [46]. Fig. 12 shows the photocurrent response of pure BMO and 3.0 at.% Tb-BMO sample during light switching on and off. Obviously, the current abruptly increases and decreases when switch the light source on and off. The 3.0 at.% Tb-BMO sample exhibited an obviously enhanced photocurrent response compared with pure BMO. It implied that a more efficient separation of the photo-generated electron–hole pairs and fast transfer of photoinduced charge carriers occurred in the 3.0 at. % Tb-BMO photocatalyst. In addition, it needs to be noted that 3.0 at.% Tb-BMO hold residual current with the light source off. This is probably attributed to the presence of the in-built Tb^{4+}/Tb^{3+} redox centers in the BMO bulk, which could release the trapped electrons or holes under thermal motion [47].

To further explore the charge process with Tb^{4+}/Tb^{3+} redox centers during the photocatalytic degradation process, the trapping experiments with different scavengers were performed with 3.0 at.% Tb-BMO composite as shown in Fig.13. In this way the active species including holes (h^+), superoxide radical ($\cdot O_2^-$) and hydroxyl radicals (·OH) with effective oxidation and reduction potential could be determined [48,49]. In the present study, the ethylenediaminetetraacetic acid disodium salt (EDTA-2Na), 1, 4-benzoquinone (BQ) and isopropyl alcohol (IPA) were utilized as

scavengers of h^+, $\cdot O_2^-$ and ·OH, respectively. Remarkably, the RhB degradation was halted once the scavenger EDTA (1 mM) for h^+ was added to the reaction system. Meanwhile, there was an obvious decline of the photodegradation rate with the addition of the scavenger BQ (1 mM) for· O_2^-. However, there was no evident decreases of the photodegradation rate of RhB when the scavenger IPA (1 mM) for ·OH was added. These results implied that h^+ and $\cdot O_2^-$ may be the major reactive species, while ·OH had little impact on the RhB photodegradation process.

The possible photocatalytic mechanism on the Tb-BMO photocatalyst under visible-light irradiation were there by proposed, as shown in Fig. 14. The photo-generated electrons could transfer to the conduction band (CB) from the valence band (VB) and the holes formed in the valence band when the semiconductor was irradiated by visible light. The Tb^{4+} is half-filled in 4*f* orbital that holds 7 *f*-electrons, and this configuration is relatively stable [50]. In this case, the photo-generated electrons in Tb-BMO were trapped by Tb^{4+} ions forming Tb^{3+}, and the trapped electrons could easily transfer to the oxygen molecules (O_2) adsorbed on the surface of the Tb-BMO catalysts due to this relatively stable configuration. Subsequently, the released electrons reacted with O_2 to generate the active species superoxide radical anion ($\cdot O_2^-$) and the Tb^{3+} ions returned to the original stable half-filled state (Tb^{4+}). Fig. 15 shows the chemical state of the terbium which was after photocatalytic reaction. The trapping and releasing process of electrons enhances the efficiency of charge transfer and separation of the photo-generated electrons and holes, which contributed to organics degradation by the active species of holes (h^+) and superoxide radical anion ($\cdot O_2^-$). Therefore, the above process indicated that the appropriate terbium doping amounts could significantly improve the photocatalytic activity of BMO via forming redox center. What's more, the results of the photoluminescence spectra, photocurrent measurement and active species trapping experiments were also in agreement with the supposed photocatalytic mechanism.

4. Conclusions

Terbium doped grass-like bismuth molybdate were successfully synthesized by a hydrothermal process. The results demonstrated that terbium dopant not only increased the visible-light absorption rang of Bi_2MoO_6, but also promoted the separation efficiency of photo-generated electron-hole pairs with appropriate addition of terbium (3.0 at.% Tb-BMO) because of the trapping-releasing process of electrons with the in-built Tb^{4+}/Tb^{3+} redox centers. Therefore, the use of Tb^{4+} /Tb^{3+} ions as a photo-induced redox center is a potential strategy for charge separation and thus improving the visible-light photocatalytic activity.

Author Information

* Corresponding author at: University of Science & Technology Beijing, Department of Chemistry, No.30 Xueyuan Rd., Haidian District, Beijing 100083, China. Tel.:+86 10 62332468.

E-mail address: wjli_ustb@163.com (W.Li).

Acknowledgment

We gratefully acknowledge the financial support provided by the Project of the National Natural Science Foundation of China (Grant No.21271022).

References

1 L. Liu, H. Zhao, J. M. Andino and Y. Li, *Acs Catal.*, 2012, 2, 1817-1828.

2 H. Hori, K. Koike, Y. Suzuki, M. Ishizuka, J. Tanaka, K. Takeuchi and Y. Sasaki, *J. Mol. Catal. A: Chem.*, 2002,179, 1-9.

3 S. U. M. Khan, M. Al-Shahry and W. B. Ingler, *Sci.*, 2002,297, 2243-2245.

4 A. Yamakata, T. Ishibashi and H. Onishi, *J. Mol. Catal. A: Chem.*, 2003,199, 85–94.

5 J. Xu, W. Meng, Y. Zhang, L. Li and C. Guo, *Appl. Catal. B: Environ.*, 2011,107, 355-362.

6 B. Pourabbas and B. Jamshidi, *Chem. Eng. J.*, 2008, 138, 55-62.

7 J. Yu and A. Kudo, Adv. Funct. *Mater.*, 2006, 16, 2163-2169.

8 H. Fu, C. Pan, W. Yao and Y. Zhu, *J. Phys. Chem. B*, 2005, 109, 22432-22439.

9 G. Tian, Y. Chen, W. Zhou, K. Pan, Y. Dong, C. Tian and H. Fu, *J. Mater. Chem.*, 2011, 21, 887-892.

10 B. Han, J. Zhang, P. Li, J. Li, Y. Bian and H. Shi, *J. Electron. Mater.*, 2015, 44, 1028-1033.

11 D. Zhou, H. Wang, X. Yao and L. Pang, *J. Am. Ceram. Soc.* 2008, 91, 3419-3422.

12 D. Zhou, C. A. Randall, H. Wang, L. Pang and X. Yao, *J. Am. Ceram. Soc.* 2010, 93, 1096-1100.

13 H. Li, K. Li and H. Wang, Mater. *Chem. Phys.*, 2009, 116, 134-142.

14 L. Zhang, T. Xu, Z. Xu and Y. Zhu, *Appl. Catal. B: Environ.*, 2010, 98, 138–146.

15 W. Yin, W. Wang and S. Sun, *Catal. Commun.*, 2010, 11, 647–650.

16 A. M. D. L. Cruz, S. O. Alfaro, E. L. Cuéllar and U. O. Méndez, *Catal. Today*, 2007, 129, 194–199.

17 Y. Xu and W. Zhang, *Dalton T.*, 2013, 42, 1094-1101.

18 Y. Chen, G. Tian, Y. Shi, Y. Xiao and H. Fu, *Appl. Catal. B: Environ.*, 2015, 164, 40-47.

19 S. Gu, W. Li, F. Wang, S. Wang, H. Zhou and H. Li, *Appl. Catal. B: Environ.*, 2015, 170, 186-194.

20 T. Yan, M. Sun, H. Liu, T. Wu, X. Liu, Q. Yan, W. Xu, B. Du, *J. Alloys Compd.*, 2015, 634, 223-231.

21 X. Zhao, J. Qu, H. Liu, Z. Qiang, R. Liu and C. Hu, *Appl. Catal. B: Environ.*, 2009, 91, 539-545.

22 T. Zhou, J. Hu and J. Li, *Appl. Catal. B: Environ.*, 2011, 110, 221–230.

23 A. Phuruangrat, S. Putdum, P. Dumrongrojthanath, N. Ekthammathat, S. Thongtem, T. Thongtem, *Mater. Sci. in Semicon. Proc.*, 2015, 34, 175-181.

24 A. Phuruangrat, A. Maneechote, P. Dumrongrojthanath, N. Ekthammathat, S. Thongtem, T.

Thongtem, *Mater. Lett.*, 2015, 159, 289-292.

25 A. A. Alemi, R. Kashfi and B. Shabani, *J. Mol. Catal. A: Chem.*, 2014, 392, 290–298.

26 K. P. Mani, G. Vimal, P. R. Biju, C. Joseph, N. V. Unnikrishnan and M. A. Ittyachen, *Spectrochim. Acta A*, 2015, 148, 412-419.

27 Y. K. Kuo, B. T. Liou, S. H. Yen and H. Y. Chu, *Opt. commun.*, 2004, 237, 363-369.

28 J. Yuan, X. Zeng, J. Zhao, Z. Zhang, H. Chen and X. Yang, *J. Phys. D: Appl. Phys.*, 2008, 41, 105406.

29 J. Y. Park, H. C. Jung, G. S. R. Raju, B. K. Moon, J. H. Jeong and J. H. King, *Solid State Sci.*, 2010, 12, 719-724.

30 F. D. Hardcastle and I. E. Wachs, *J. Phys. Chem.*, 1991, 95, 10763-10772.

31 R. Adhikari, G. Gyawali, S. H. Cho, R. Narro-Garcia, T. Sekino and S. W. Lee, *J. Solid State Chem.*, 2014, 209, 74-81.

32 C. Kongmark, R. Coulter, S. Cristol, A. Rubbens, C. Pirovano, A. Lofberg, G. Sankar, W. V. Beek, E. Bordes-Richard and R. N. Vannier, *Cryst. Growth Des.*, 2012, 12, 5994-6003.

33 S. Gu, W. Li, F. Wang, H. Li and H. Zhou, *Catal. Sci. Technol.*, 2015, DOI: 10.1039 /C5CY01412C

34 C. Xu, P. Zhang and L. Yan, *J. Raman Spectrosc*, 2001, 32, 862-865.

35 B. M. Sanchez, T. Brousse, C. R. Castro, V. Nicolosi and P. S. Grant, *Electrochim. Acta*, 2013, 91, 253–260.

36 A. Phuruangrat, N. Ekthammathat, B. Kuntalue, P. Dumrongrojthanath, S. Thongtem and T. Thongtem, *J. Nanomater.*, 2014, DOI: 10.1155/2014/934165.

37 A. B. Hungria, A. Martínez-Arias, M. Fernández-García, A. Lglesias-Juez, A. Guerrero-Ruiz, J. J. Calvino, J. C. Conesa and J. Soria, *Chem. mater.*, 2003, 15, 4309-4316.

38 H. Fu, C. Pan, W. Yao and Y. Zhu, *J. Phys. Chem. B*, 2005, 109, 22432-22439.

39 Z. Ma, J. Zhou, Z. Chen and E. Xie, *Dlam. Relat. Mater.,* 2011, 20, 475-479.

40 D. D. Sarma and C. N. R. Rao, *J. Electron Spectrosc.*, 1980, 20, 25-45.

41 G. Blanco, J. M. Pintado, S. Bernal, M. A. Cauqui, M. P. Corchado, A. Galtayries, J. Ghijsen, R. Sporken, T. Eickhoff and W. Drube, *Surf. Interface Anal.*, 2002, 34, 120-124.

42 Y. Luo, G. Tan, G. Dong, H. Ren and A. Xia, *Ceram. Int.*, 2015, 41, 3259–3268.

43 C. Guo, J. Xu, S. Wang, L. Li, Y. Zhang and X. Li, *CrystEngComm*, 2012, 14, 3602-3608.

44 M. Andersson, L. Osterlund, S. Ljungstrom and A. Palmqvist, *J. Phys. Chem. B*, 2002, 106, 10674-10679.

45 H. Huang, X. Han, X. Li, S. Wang, P. Chu and Y. Zhang, *Acs Appl. Mater. Inter.*, 2014, 7, 482-492.

46 F. Wang, W. Li, S. Gu, H. Li, H. Zhou and X. Wu, *RSC Adv.*, 2015, 5, 89940-89950.

47 A. Bessiere, S. Sharma, N. Basavaraju, K. Priolkar, L. Binet, B. Viana, A. Bos, T. Maldiney, C. Richard, D. Scherman and D. Gourier, *Chem. Mater.*, 2014, 26, 1365–1373.

48 H. Huang, L. Liu, Y. Zhang and N. Tian, *J. Alloys Compd.*, 2015, 619, 807-811.

49 W. Chen, G. Duan, T. Liu, S. Chen and X. Liu, *Mater. Sci. in Semicon. Proc.*, 2015, 35, 45-54.

50 N. Tian, Y. Zhang, H. Huang, Y. He and Y. Guo, *J. Phys. Chem. C*, 2014, 118, 15640−15648.

Abstract A series of terbium-doped Bi_2MoO_6 with different Tb content were synthesized using a hydrothermal method. Crystalline structure, surface area, morphology, chemical state and optical properties were analyzed in detail. The photocatalytic activity of the samples were evaluated by degrading organics under visible light irradiation. The results indicated that doping of terbium ions could obviously improve the photocatalytic activity of Bi_2MoO_6, which was attributed to the generation of Tb^{4+} /Tb^{3+} redox centers in terbium-doped Bi_2MoO_6. The photoluminescence (PL) spectroscopy, photocurrent measurement and active species trapping experiments suggest that the recombination of photo-generated electron-hole pairs was efficiently restrained by trapping-releasing process between Tb^{4+} and Tb^{3+} ions.